Two-dimensional spectroscopy of two-dimensional materials: A Mahan-Nozières-De Dominicis model of electron-exciton scattering

Lachlan P. Lindoy,[1] Yao-Wen Chang,[2] and David R. Reichman[1,*]
[1]*Department of Chemistry, Columbia University, 3000 Broadway, New York, New York 10027, USA*
[2]*Physics Division, National Center for Theoretical Sciences, Taipei 10617, Taiwan*

(Received 2 August 2022; revised 2 October 2022; accepted 7 October 2022; published 8 December 2022)

In this paper, we provide a systematically convergable and efficient numerical approach to simulate multitime correlation functions in the Mahan-Nozières-De Dominicis model, which crudely mimics the spectral properties of doped two-dimensional (2D) semiconductors such as monolayer transition metal dichalcogenides. We apply this approach to study the coherent 2D electronic spectra of the model. We show that several experimentally observed phenomena, such as peak asymmetry and coherent oscillations in the waiting-time dependence of the trion-exciton cross peaks of the 2D rephasing spectrum, emerge naturally in our approach. Additional features are also present which find no correspondence with experimentally expected behavior. We trace these features to the infinite hole mass property of the model. We use this understanding to construct an efficient approach which filters out configurations associated with the lack of exciton recoil, enabling the connection to previous work and providing a route to the construction of realistic 2D spectra over a broad doping range in 2D semiconductors.

DOI: 10.1103/PhysRevB.106.235407

I. INTRODUCTION

Over the last decade, the study of two-dimensional (2D) semiconductors and heterostructures constructed from them has greatly enhanced our understanding of fundamental quasiparticle excitations such as excitons, trions, and biexcitons, and it has opened a path toward the construction of optoelectronic devices [1–3]. Among this class of materials, transition metal dichalcogenides (TMDCs) stand out due to the reliability with which they can be created and manipulated. Their unique physical properties, such as large spin-orbit coupling and distinguished spin and valley degrees of freedom, create an ideal playground for the observation of physical phenomena [4–10]. Indeed, a variety of experimental approaches have been employed to reveal behavior ranging from the individual properties of dark excitons to collective behavior such as Wigner crystallization and exciton condensation [11–16].

One experimental technique that has been applied to the study of TMDCs is 2D electronic spectroscopy [17–19]. In principle, 2D spectroscopy has the potential to uncover properties such as coherent coupling between excitations that cannot be revealed via linear optical techniques such as absorption or photoluminescence. On the other hand, 2D spectroscopy can be difficult to perform and interpret and often requires a complimentary theory to unlock its full potential. In the latter regard stands the important work of Tempelaar and Berkelbach [20], who presented a detailed, microscopic theory of 2D spectra in TMDCs. One possible limitation of their approach, however, is the fact that it is confined to a regime of relatively low electron doping. Authors of recent work have emphasized the important role played by collective dressing of excitons by excess electrons in the higher doping regime, where the trion peak may be interpreted as emerging from a lower energy branch of a collective exciton-polaron spectrum [21,22].

In this paper, we aim to enhance our understanding of the emergent features in the 2D spectra of 2D semiconductors by considering a simple model for which exact simulation (i.e., the simulations are systematically convergable toward the exact solution) of the various 2D signals is possible [23,24]. The downside of such an approach is that the model is less realistic than that studied in Ref. [20], but the advantage is that the calculations are nonperturbative and thus can describe the evolution over the full doping range. Interestingly, we find that several features that arise from our calculations agree with expectations from experiments and past work, while some do not. A closer examination of the spectral features which appear unique to our approach enable the facile elimination of these features and afford a direct link to the work of Ref. [20]. This bridge between our phenomenological approach and past microscopic ones should enable the future construction of theoretical tools for the description of nonlinear 2D spectra that contain microscopic information but are still capable of capturing nonperturbative effects at high doping [25].

Our paper is organized as follows. In Sec. II, the theory of 2D coherent electron spectroscopy for a simple model of 2D semiconductors, a Mahan-Nozières-De Dominicis (MND) Hamiltonian-based model of electron-exciton scattering, is presented. In Sec. III, the 2D rephasing spectra obtained from this theory are presented, the various features observed are compared against previous theoretical and experimental spectra, and the origin of the features present in the spectra are discussed. Section IV provides a summary and outlook.

*drr2103@columbia.edu

II. 2D SPECTROSCOPY OF A MND MODEL FOR 2D SEMICONDUCTORS

A. MND Hamiltonian for electron-exciton scattering

We will consider an idealized model for describing electron-exciton scattering in electron-doped semiconductors. We take an electron-exciton scattering Hamiltonian of the form of the MND Hamiltonian [25–27]:

$$\hat{H} = \mathcal{E}\hat{X}^\dagger\hat{X} + \sum_{\mathbf{k}} \epsilon_{\mathbf{k}} \hat{c}_{\mathbf{k}}^\dagger \hat{c}_{\mathbf{k}} + \sum_{\mathbf{k}\mathbf{k}'} V_{\mathbf{k}\mathbf{k}'} \hat{c}_{\mathbf{k}}^\dagger \hat{c}_{\mathbf{k}'} \hat{X}^\dagger \hat{X}. \tag{1}$$

Here, $\hat{X}^\dagger$ and $\hat{X}$ are creation and annihilation operators for an immobile exciton, $\hat{c}_{\mathbf{k}}^\dagger$ and $\hat{c}_{\mathbf{k}}$ are creation and annihilation operators for an electron in the conduction band with quasimomentum $\mathbf{k}$, $\mathcal{E}$ is the exciton transition energy, $\epsilon_{\mathbf{k}} = |\mathbf{k}|^2/2m_e$ is the electron kinetic energy with m_e the electron mass, and $V_{\mathbf{k}\mathbf{k}'}$ the scattering potential.

Assuming a $1s$ exciton state, we take the scattering potential to be [25]

$$V_{\mathbf{k}\mathbf{k}'} = \frac{-v_{\mathbf{k}-\mathbf{k}'}}{A}\left[1 - \exp\left(-\frac{1}{2}|\mathbf{k}-\mathbf{k}'|^2\zeta^2\right)\right], \tag{2}$$

where ζ is the exciton radius, A is the area, and $v_{\mathbf{k}-\mathbf{k}'}$ is the screened Coulomb potential and here is taken to be the Rytova-Keldysh potential [28–30]:

$$v_{\mathbf{k}-\mathbf{k}'} = \frac{2\pi e^2}{|\mathbf{k}-\mathbf{k}'|(1 + r_0|\mathbf{k}-\mathbf{k}'|)}, \tag{3}$$

where r_0 is the screening length. We note that this form of the potential is microscopically derived in the limit of infinite exciton effective mass, which is the correct limit for the MND model [31]. If, however, we endeavor to more realistically treat the nearly equal electron and hole masses as found in TMDCs, a different effective potential should be employed [32].

Within this model, electron doping may be included by considering an initial electron distribution ($n_{\mathbf{k}}$) given by a 2D noninteracting electron gas with

$$n_{\mathbf{k}} = \frac{1}{\exp\left[\beta(\epsilon_{\mathbf{k}} - \epsilon_f)\right] + 1}, \tag{4}$$

where ϵ_f is the Fermi energy, and β the inverse temperature. In the zero temperature limit, this reduces to

$$n_{\mathbf{k}} = 1 - \Theta(\epsilon_{\mathbf{k}} - \epsilon_f). \tag{5}$$

This model ignores spin degrees of freedom and exchange interactions and, as mentioned above, assumes a single, immobile (infinite mass) exciton with a purely $1s$ character that couples to a noninteracting Fermi sea. As such, it is not expected to quantitatively describe experimental results. However, this model can qualitatively capture the emergence of a trion peak, oscillator strength transfer, and doping-dependent line shapes in the linear absorption spectrum of monolayer TMDCs even at relatively high electron doping [25]. Here, we employ this simplified model to gain insight into the nonlinear 2D spectrum of 2D materials such as TMDCs, including its doping dependence. While limited, the depth with which we can investigate physical features enables an understanding of the more realistic microscopic situation probed in real experiments.

B. Multitime correlation functions

Here, 2D coherent spectroscopy provides a means of monitoring coherent and incoherent dynamics of a system. This technique employs a sequence of three ultrafast pulses to produce a nonlinear optical response in the material [17,33]. By measuring this response and its dependence on the timing between pulses, it is possible to resolve couplings between distinct states in the system and to differentiate between coherent and incoherent energy transfer processes [17,34].

For the electron–single immobile exciton scattering model, we consider here the light-matter interaction operator takes the form [25]:

$$\hat{V} = c^*\hat{X}^\dagger + c\hat{X}, \tag{6}$$

where c is a scalar proportional to the transition momentum matrix element. With this definition and within the rotating wave approximation, a total of four distinct multitime correlation functions (and their complex conjugates) can provide significant contributions to the nonlinear optical response of this model [33]. These are the nonrephasing stimulated emission R_1, the rephasing stimulated emission R_2, the rephasing ground state bleach R_3, and the nonrephasing ground state bleach R_4 contributions. In principal, additional multitime correlation functions that contain contributions from states with more than a single excited exciton could be probed through 2D coherent spectroscopy experiments. Here, for simplicity and to allow for qualitative comparisons with previously obtained experiments [17], we only consider the two rephasing contributions which are given by

$$R_2(t_1,t_2,t_3) = \mathrm{Tr}[\hat{V}(t_1+t_2)\hat{V}(t_1+t_2+t_3)\hat{V}(t_1)\hat{\rho}\hat{V}], \tag{7}$$

$$R_3(t_1,t_2,t_3) = \mathrm{Tr}[\hat{V}(t_1)\hat{V}(t_1+t_2+t_3)\hat{V}(t_1+t_2)\hat{\rho}\hat{V}]. \tag{8}$$

The corresponding 2D rephasing spectrum can be obtained from this correlation functions as

$$S_{\mathrm{RP}}(\omega_1,t_2,\omega_3) = S_2(\omega_1,t_2,\omega_3) + S_3(\omega_1,t_2,\omega_3), \tag{9}$$

where

$$S_i(\omega_1,t_2,\omega_3) = \int_0^\infty dt_1 \exp(-i\omega_1 t_1) \times \int_0^\infty dt_3 \exp(i\omega_3 t_3) R_i(t_1,t_2,t_3), \tag{10}$$

for $i = 2, 3$. Here, ω_1 and ω_3 are the excitation and emission energies, respectively, and t_2 is the waiting time. In Fig. 1, we illustrate the quantum mechanical pathways that contribute to this spectrum. Similar expressions can be obtained for the nonrephasing pathways. A treatment of pathways involving states with more than a single excited exciton would require an extension of the MND model discussed in Sec. II A.

C. 2D spectroscopy of the MND model

If we assume that the system is initially in a state with no exciton and with an initial thermal (or ground state if at zero temperature) configuration of the conduction electrons, it becomes possible to efficiently evaluate the multitime correlation functions [given in Eqs. (7) and (8)] for the electron-exciton scattering form of the MND model. A given

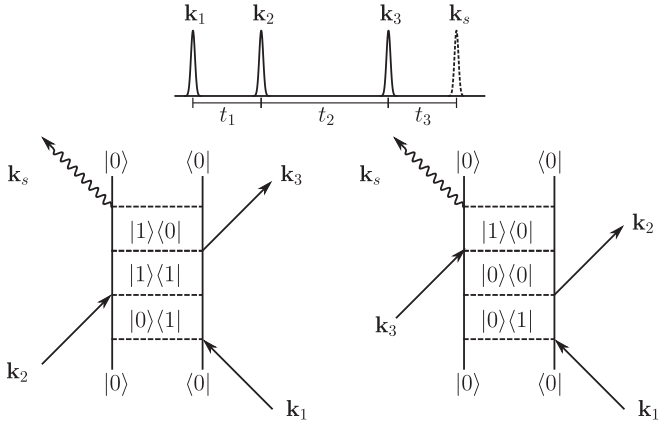

FIG. 1. Illustration of the pulse time ordering used for obtaining two-dimensional (2D) rephasing spectra (top). The double-sided Feynman diagrams representing the Liouville space pathways that contribute to the 2D rephasing spectrum (bottom). These contributions are accounted for by the correlation functions $R_2(t_1, t_2, t_3)$ (left) and $R_3(t_1, t_2, t_3)$ (right) and correspond to stimulated emission and ground state bleach spectra, respectively. Here, we have used $|0\rangle$ and $|1\rangle$ to represent zero and one exciton states, respectively, and at each stage, arbitrary configurations of the conduction band electrons are allowed.

multitime correlation function can be expressed as

$$R_i(t_1, t_2, t_3) = \det[(\mathbf{1} - \mathbf{n}) + \mathbf{n}\mathbf{R}_i(t_1, t_2, t_3)], \tag{11}$$

where $\mathbf{1}$ is the identity matrix, and $\mathbf{n}$ is the matrix with elements $[\mathbf{n}]_{\mathbf{k}\mathbf{k}'} = \delta_{\mathbf{k}\mathbf{k}'} n_{\mathbf{k}}$. Restricting ourselves to the rephasing contributions, we have

$$\begin{aligned}\mathbf{R}_2(t_1,t_2,t_3) = {} & \mathbf{\Phi} \exp[i\tilde{\boldsymbol{\epsilon}}(t_1 + t_2)]\mathbf{\Phi}^\dagger \exp(i\boldsymbol{\epsilon} t_3) \\ & \times \mathbf{\Phi} \exp[-i\tilde{\boldsymbol{\epsilon}}(t_2 + t_3)]\mathbf{\Phi}^\dagger \exp(-i\boldsymbol{\epsilon} t_1),\end{aligned} \tag{12}$$

$$\begin{aligned}\mathbf{R}_3(t_1,t_2,t_3) = {} & \mathbf{\Phi} \exp(i\tilde{\boldsymbol{\epsilon}} t_1)\mathbf{\Phi}^\dagger \exp[i\boldsymbol{\epsilon}(t_2 + t_3)] \\ & \times \mathbf{\Phi} \exp(-i\tilde{\boldsymbol{\epsilon}} t_3)\mathbf{\Phi}^\dagger \exp[-i\boldsymbol{\epsilon}(t_1 + t_2)],\end{aligned} \tag{13}$$

where $\boldsymbol{\epsilon}$ is a matrix with elements $[\boldsymbol{\epsilon}]_{\mathbf{k}\mathbf{k}'} = \delta_{\mathbf{k}\mathbf{k}'}\epsilon_{\mathbf{k}}$, and $\mathbf{\Phi}$ and $\tilde{\boldsymbol{\epsilon}}$ are obtained by solving the eigenvalue problem:

$$\sum_{\mathbf{k}\mathbf{k}'} [(\epsilon_{\mathbf{k}} + \mathcal{E})\delta_{\mathbf{k}\mathbf{k}'} + V_{\mathbf{k}\mathbf{k}'}]\Phi_{\mathbf{k}'n} = \Phi_{\mathbf{k}n}\tilde{\epsilon}_n. \tag{14}$$

In the zero temperature limit, Eq. (11) reduces to

$$R_i(t_1, t_2, t_3) = \det[\mathbf{R}_i(t_1, t_2, t_3)]_{\epsilon_{\mathbf{k}} \leq \epsilon_f}, \tag{15}$$

where the determinant is only evaluated over the rows and columns of the matrix $\mathbf{R}_i$ with $\epsilon_{\mathbf{k}}$ less than or equal to the Fermi energy. Similar expressions can be obtained for the nonrephasing contributions.

D. Computational details

Before we can numerically evaluate Eqs. (12), (13), and (15), it is necessary to specify a discretization of the model. We use a finite-sized square box with square lattice points given by

$$\mathbf{k} = (k_x, k_y) = \left\{ \frac{\pi[2\kappa_x - (N-1)]}{L}, \frac{\pi[2\kappa_y - (N-1)]}{L} \right\}, \tag{16}$$

where $\kappa_x, \kappa_y = 0, 1, \ldots, N-1$. Here, N is the number of grid points in one direction, and $L = Na_\Delta$ is the box length, where a_Δ is a cutoff length that is set by the choice of a cutoff energy $E_\Delta = \max(k_x^2/2m_e)$ (here taken to be $E_\Delta = 1$ eV). We have used $N = 140$ grid points per dimension for all calculations presented here.

In our calculations, we have chosen the screening length, electron mass, and exciton transition energy consistent with those of $MoSe_2$. We have taken a screening length of $r_0 = 51.7$ Å (obtained from the 2D polarizability used in Ref. [20] obtained via the approximate relation $r_0 = 2\pi\chi_{2d}$) [10], electron mass of $m_e = 0.52m_0$ [35], and exciton transition energy $\mathcal{E} = 1.66$ eV [20]. As was the case in Ref. [25], the exciton radius $\zeta = 8$ Å was taken as an adjustable parameter that was used to control the trion-binding energy. We again emphasize, however, that the form of our exciton-electron scattering potential is only consistent in the limit $m_{\text{ex}} \to \infty$, a situation distinct from that of typical TMDCs [32].

To compute the 2D rephasing spectrum (Eq. 9) for a given waiting time, it is necessary to evaluate the two rephasing multitime correlation functions over a dense set of time points (t_1, t_3). We have used a 2000×2000 grid of points (t_1, t_3) to obtain the spectra presented here. For each time point, we need to construct the two $(N^2 \times N^2)$ dense matrices $\mathbf{R}_2$ and $\mathbf{R}_3$ for which we need to evaluate the determinant. For the large matrices and grid sizes considered here, this process can be rather costly; however, it can be rendered significantly more efficient via GPU acceleration. All results presented here were obtained using a GPU implementation of Eqs. (12), (13), and (15).

III. 2D REPHASING SPECTRA

A. Doping-dependent 2D rephasing spectra

In Fig. 2, we present the linear absorption spectra and absolute value of the 2D rephasing spectra obtained with a waiting time $t_2 = 0$, at zero temperature, and for varying values of the Fermi energy ϵ_f. Consistent with previous experimental and theoretical studies [17,20], each spectrum shows four peaks arranged in a square pattern, readily attributed to the bound trion and exciton states. The significant asymmetry that is observed in the line shapes of the linear absorption spectra [25] is evident in the 2D spectra as the long tails of the peaks (most evident in the exciton-exciton peak).

As the Fermi energy increases, there is considerable oscillator strength transfer from the exciton-exciton peak to the trion-trion peak, consistent with the linear spectra [25]. The two cross peaks, corresponding to excitation at the exciton(trion) and emission at the trion(exciton) energies which we will refer to as the X-X^-(X^--X), are more significant as the Fermi energy increases, becoming the dominant feature at $\epsilon_f = 10$ meV. Additionally, as the Fermi energy increases, it becomes possible to resolve an additional peak (that for smaller Fermi energies appears as a shoulder in the

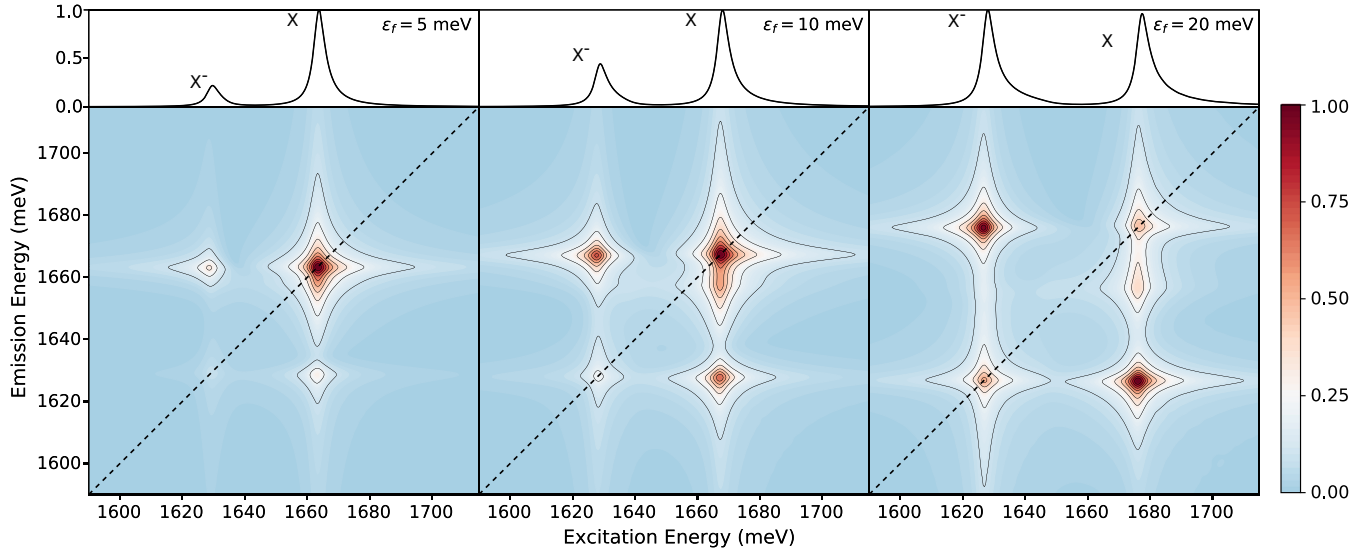

FIG. 2. Doping dependence of the linear absorption spectrum and the amplitude two-dimensional (2D) rephasing spectrum of the Mahan-Nozières-De Dominicis (MND) model calculated with a waiting time of $t_2 = 0$. Here, we have normalized each of the 2D amplitude spectra so that the maximum amplitude is 1. The dashed line along the diagonal corresponds to $\omega_1 = \omega_3$ (excitation energy = emission energy).

exciton-exciton peak). We discuss the origin of this peak in Sec. III B. The presence of the cross peaks in the spectra is indicative of exciton-trion coupling. Such peaks can arise from both coherent and incoherent processes. To distinguish between these distinct mechanisms, it is necessary to consider 2D spectra evaluated for different values of the waiting time t_2. In Fig. 3, we present the absolute value of the 2D rephasing spectrum at varying values t_2 for a Fermi energy of $\epsilon_f =$ 10 meV. The diagonal peaks remain relatively unchanged. In contrast, oscillations are observed in the amplitudes of the cross peaks, with the amplitudes significantly diminished at $t_2 = 60$ fs compared with either $t_2 = 0$ or 120 fs. This behavior is qualitatively consistent with the experimental 2D rephasing spectrum obtained for $MoSe_2$ [17]. In addition to this, we note that the intensity of the shoulder peak decreases with increasing waiting time.

The oscillation in the amplitude of the cross peaks is made more explicit in Fig. 4, where we present the waiting-time-dependent amplitude of the X-X^- and X^--X cross peaks for the MND model with $\epsilon_f = 5$ and 10 meV. Here, we observe well-defined oscillations in the peak amplitudes supporting the fact that the system undergoes coherent interconversion between exciton and trion states, as well as a decay with time, consistent with experimental spectra [17]. The frequency of the oscillation in the cross peaks increases with increasing Fermi energy ϵ_f due to the increase in the energy splitting between the exciton peak and the trion peak with increasing doping. Additionally, significant asymmetry in the X-X^- and X^--X peak amplitudes is observed, in contrast to the spectra of Ref. [20]. In the next section, we will explore the origin of this asymmetry and of the additional peak observed in the spectra.

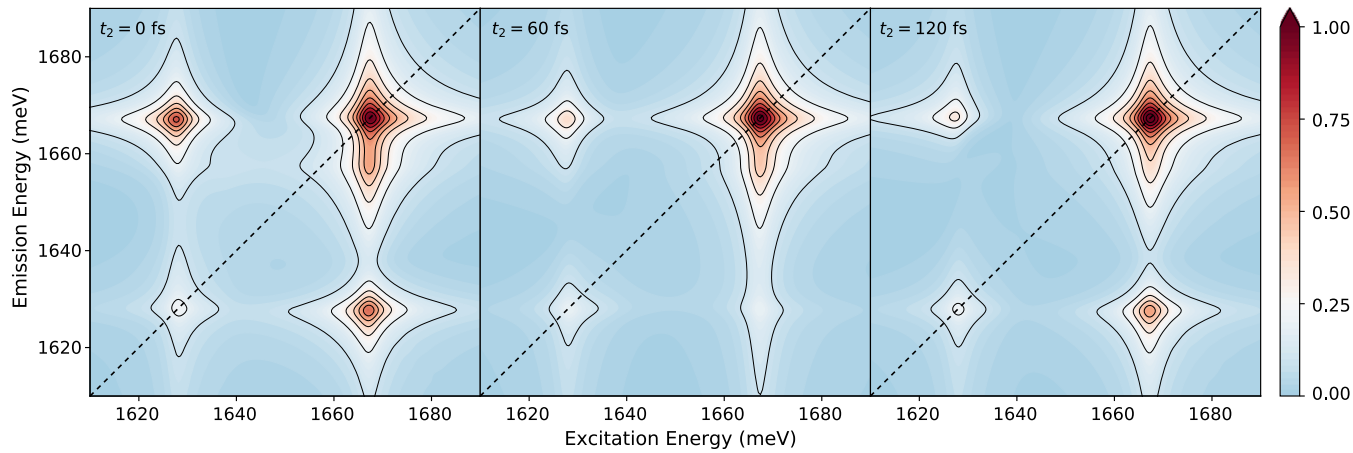

FIG. 3. Amplitude two-dimensional (2D) rephasing spectrum of the Mahan-Nozières-De Dominicis (MND) model with $\epsilon_f = 10$ meV calculated for a range of waiting times t_2 (shown on each panel). Here, each of the 2D amplitude spectra have been normalized by the amplitude of the largest peak of the $t_2 = 0$ spectrum. The dashed line along the diagonal corresponds to $\omega_1 = \omega_3$.

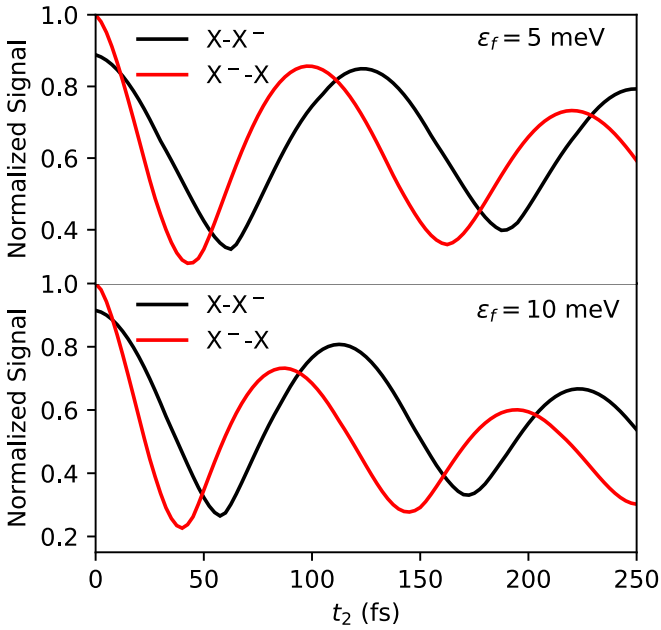

FIG. 4. The waiting time t_2, dependent normalized amplitude of the two-dimensional (2D) rephasing spectrum at the lower (X-X^-) and upper (X^--X) cross peaks obtained for the Mahan-Nozières-De Dominicis (MND) model with $\epsilon_f = 5$ (top) and 10 (bottom) meV. The two curves in each panel have been normalized by the same constant so that the maximum value obtained by either of the curves is 1.

B. Restricted final state spectra

In addition to the expected four peaks that can be attributed to the bound trion and exciton states and coherences between them, the 2D rephasing spectra shown in Fig. 2 exhibit an additional peak at large doping corresponding to excitation at the exciton energy followed by emission at an energy between the exciton and trion energies. The identification of the origin of this peak in the 2D spectra is complicated by the large number of distinct Liouville space pathways that contribute to the 2D rephasing spectra. While the state of the exciton following the application of a pulse is restricted to those shown in Fig. 1, the conduction electrons are free to take any dynamically allowed configuration.

In an effort to obtain a better understanding of the source of the additional peak observed in the 2D rephasing spectra at high Fermi energies, we restrict the possible Liouville space pathways by restricting the final configuration of the conduction electrons. This can be done by replacing the light-matter interaction term at time $t_1 + t_2 + t_3$ in Eqs. (7) and (8) with a new term that involves a projection onto the desired final conduction electron state $|\Psi_f\rangle$, that is,

$$\hat{V}(t_1+t_2+t_3) \rightarrow \hat{V}_f(t_1+t_2+t_3), \tag{17}$$

with

$$\hat{V}_f = \hat{V} \otimes |\Psi_f\rangle\langle\Psi_f|. \tag{18}$$

Here, we will note that, at $t_2 = 0$, the two contributions to the rephasing spectra are equivalent, and we thus only provide explicit results for rephasing stimulated emission correlation function R_2:

$$R_2^f(t_1,t_2,t_3) = \det\left\{\mathbf{M}^{(1)}_{[\mathbf{k}_0][\mathbf{k}_f]}(t_1,t_2,t_3)\mathbf{M}^{(2)}_{[\mathbf{k}_f][\mathbf{k}_0]}(t_1,t_2,t_3)\right\}, \tag{19}$$

where

$$\mathbf{M}^{(1)}(t_1,t_2,t_3) = \mathbf{\Phi}\exp[i\tilde{\boldsymbol{\epsilon}}(t_1+t_2)]\mathbf{\Phi}^\dagger\exp(i\boldsymbol{\epsilon}t_3), \tag{20}$$

$$\mathbf{M}^{(2)}(t_1,t_2,t_3) = \mathbf{\Phi}\exp[-i\tilde{\boldsymbol{\epsilon}}(t_2+t_3)]\mathbf{\Phi}^\dagger\exp(-i\boldsymbol{\epsilon}t_1), \tag{21}$$

and we have used the notation $\mathbf{A}_{[\mathbf{a}][\mathbf{b}]}$ to denote the matrix formed from the rows $\mathbf{a}$ and columns $\mathbf{b}$ of the matrix $\mathbf{A}$. Related expressions hold for the other three multitime correlation functions.

Constraining the final state of the conduction electrons to be the ground state, we can obtain the 2D-rephasing spectrum using R_2^0. At $t_2 = 0$, this spectrum is identical to the non-rephasing stimulated emission spectrum with the final state constrained to be in the ground state, which is the spectrum that was considered in Ref. [20]. In Fig. 5, we present this constrained rephasing spectrum for a waiting time of $t_2 = 0$ and for a range of Fermi energies. As with the full spectrum present in Fig. 2, the asymmetric line shapes of the one-dimensional spectra are strongly reflected by the shapes of the peaks in the 2D spectra, and these spectra capture most of the transfer of oscillator strength from the exciton to trion peak with increasing Fermi energy. Additionally, these ground state restricted spectra are symmetric around the line $\omega_1 = \omega_3$, consistent with the results in Ref. [20]. This is a consequence of restricting the final state of the bath; it follows immediately from Eq. (19). As a result, the asymmetry present in the full spectra is not observed when the final states of the conduction electrons is constrained to the ground state. The additional peak (and asymmetry in the cross peaks) arise from pathways in which, following the application of the three pulses and subsequent emission from the sample, there is at least one conduction electron that has been excited out of the Fermi sea. The remaining question is: Which states give rise to this peak?

Now, it is clearly impractical to perform an exhaustive search of all final states, as there are too many individual states, and it is not immediately clear that a contribution from a given state will necessarily correspond to a feature in the spectrum. As such, we now turn to looking at the contributions to the spectra from pathways ending in states with a specific number of excitations of the Fermi sea.

For the set of all states that contain a single excitation of a conduction electron from the Fermi sea, the modified light-matter interaction that is to be employed is

$$\hat{V}_f = \hat{V} \otimes \sum_{i\in\mathbf{k}_0}\sum_{j\in\backslash\mathbf{k}_0} \hat{c}_j^\dagger\hat{c}_i|\Psi_0\rangle\langle\Psi_0|\hat{c}_i^\dagger\hat{c}_j, \tag{22}$$

where the sum over i runs over the set of all K initially occupied orbitals $\mathbf{k}_0$ and j over the set of all unoccupied orbitals, here denoted by $\backslash\mathbf{k}_0$. Introducing the notation $\mathbf{k}_i^j$ to denote the set of orbitals occupied by $\hat{c}_j^\dagger\hat{c}_i|\Psi_0\rangle$, the singly excited state restricted multitime correlation functions may be

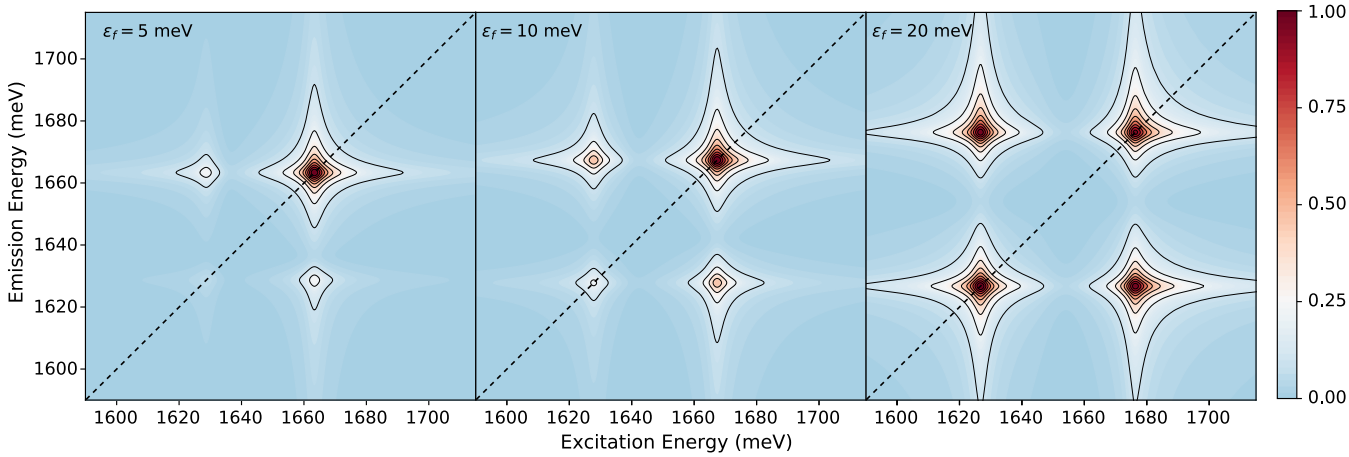

FIG. 5. Amplitude two-dimensional (2D) rephasing spectrum of the Mahan-Nozières-De Dominicis (MND) model with the final state of the conduction electrons restricted to the ground state configuration at a waiting time $t_2 = 0$ and with varying Fermi energies. The dashed line along the diagonal corresponds to $\omega_1 = \omega_3$.

expressed as

$$R_2^{(1)}(t_1,t_2,t_3) = \sum_{i\in\mathbf{k}_0}\sum_{j\notin\mathbf{k}_0} \det\left\{\mathbf{M}^{(1)}_{[\mathbf{k}_0][\mathbf{k}_i^j]}(t_1,t_2,t_3)\right\} \times \det\left\{\mathbf{M}^{(2)}_{[\mathbf{k}_i^j][\mathbf{k}_0]}(t_1,t_2,t_3)\right\}. \tag{23}$$

Given the potentially large number terms in each of these sums, evaluation of this expression is infeasible. Instead, we note that, with some rearrangement and the use of the Cauchy-Binet formula, the sum over j may be performed analytically, giving

$$R_2^{(1)}(t_1,t_2,t_3) = \sum_{i\in\mathbf{k}_0}\left\{\det\left[\mathbf{R}_2^{(i)}(t_1,t_2,t_3)\right]\right\} - KR_2^0(t_1,t_2,t_3). \tag{24}$$

Here, $\mathbf{R}_2^{(i)}(t_1,t_2,t_3)$ is a $(2K-1)\times(2K-1)$ matrix of the form:

$$\mathbf{R}_2^{(i)}(t_1,t_2,t_3) = (-1)^{K-1}\begin{bmatrix}\mathbf{0}_{(K-1)\times(K-1)} & \mathbf{A}(t_1,t_2,t_3)\\ \mathbf{B}(t_1,t_2,t_3) & \mathbf{C}(t_1,t_2,t_3)\end{bmatrix}, \tag{25}$$

where $\mathbf{0}_{(K-1)\times(K-1)}$ is the $(K-1)\times(K-1)$ matrix of zeros, and the matrices $\mathbf{A}$, $\mathbf{B}$, and $\mathbf{C}$ are the $(K-1)\times K$, $K\times(K-1)$, and $K\times K$ matrices:

$$\mathbf{A}(t_1,t_2,t_3) = \mathbf{M}^{(2)}_{[\mathbf{k}_0\setminus i][\mathbf{k}_0]}(t_1,t_2,t_3), \tag{26}$$

$$\mathbf{B}(t_1,t_2,t_3) = \mathbf{M}^{(1)}_{[\mathbf{k}_0][\mathbf{k}_0\setminus i]}(t_1,t_2,t_3), \tag{27}$$

$$\mathbf{C}(t_1,t_2,t_3) = \mathbf{M}^{(1)}_{[\mathbf{k}_0][\setminus\mathbf{k}_0]}(t_1,t_2,t_3)\mathbf{M}^{(2)}_{[\setminus\mathbf{k}_0][\mathbf{k}_0]}(t_1,t_2,t_3), \tag{28}$$

where $[\mathbf{k}_0 \setminus i]$ denotes the set of $K-1$ indices obtained after removing i from the set $\mathbf{k}_0$. In Fig. 6, we compare the real

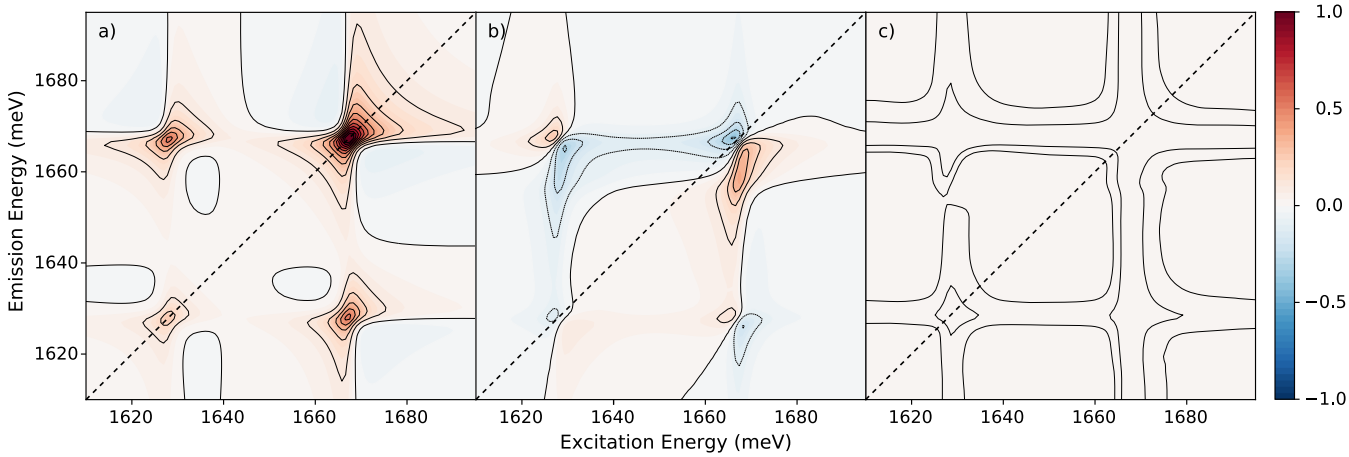

FIG. 6. Real part of the two-dimensional (2D) rephasing spectrum of the Mahan-Nozières-De Dominicis (MND) model for $\epsilon_f = 10$ meV and a waiting time $t_2 = 0$ with (a) the final state of the conduction electrons restricted to the ground state configuration, (b) all singly excited state configurations, and (c) all higher excitation configurations. Here, each spectrum is normalized by the normalization constant required to ensure that the peak in the full amplitude spectrum has amplitude 1. Note, we have used a finer spacing of contour lines in (c) to better show the structure in the spectrum. The dashed line corresponds to $\omega_1 = \omega_3$.

parts of the $t_2 = 0$ rephasing spectra obtained with (a) the final state constrained to the ground state of the conduction electron bath, (b) the set of all singly excited states, and (c) the remaining contributions coming from all final states with more than a single excitation for a system with a Fermi energy of $\epsilon_f = 10$ meV. From panel (a), we observe that the dominant contributions to the peaks arising from the exciton, trion, and their coherences can be attributed to pathways in which the conduction electrons return to their final state. The singly excited state contributions shown in panel (b) introduce asymmetry to the spectra, providing small contributions to each of the peaks present in the ground state spectra, and introduce the additional peak. All pathways in which the final state of the conduction electron bath contains more than a single excitation above the Fermi sea provide very minor changes to the spectra.

These results demonstrate that the presence of the additional peak and asymmetry in the 2D spectra can entirely be attributed to terms in which, following the three-pulse sequence and emission of a photon, the system returns to a state with no exciton but with a single conduction electron excited above the Fermi sea. Now such a state will in general have a different linear momentum from the initial configuration of the system, and so for realistic 2D coherent spectroscopy experiments (in which conservation of photon momentum and therefore the system momentum is used to resolve different pathways), these states should not contribute to the spectrum.

Within the electron-exciton scattering form of the MND Hamiltonian [Eq. (1)], the presence of such features is not surprising. In arriving at this model, it is necessary to take the infinite exciton mass limit. Upon doing so, the original scattering model becomes an impurity model that does not preserve linear momentum during interactions between the conduction electrons and exciton. As such, we can view this feature as an artifact of the immobile exciton model. It is important to note that, consistent with the above discussion, the physically filtered case [Fig. 6(a)] looks nearly identical to the spectrum obtained in a different manner in Ref. [20], where the mass of the exciton is finite.

IV. CONCLUSIONS

In this paper, we have applied a MND Hamiltonian based model of electron-exciton scattering to the evaluation of 2D spectroscopy for 2D materials. This simple model, in which we assume that the exciton is immobile, qualitatively captures many of the features that have been observed in experimental and previous theoretical treatments of the multidimensional spectroscopy of monolayer TMDCs. Furthermore, the fact that the model is solved in a numerically exact manner enables the treatment of high doping density. This numerically exact solution is facilitated by the use of GPUs, which greatly increases the efficiency of the the evaluation and manipulation of the large determinants that arise in the theory.

In making the immobile exciton approximation, the dynamics arising from this model do not conserve linear momentum. As a consequence, the resultant 2D spectra contains an additional peak that arises from pathways that result in a singly excited final state of the conduction electrons. We can effectively remove these pathways via a modification of the light-matter interaction. Once so modified, the resulting 2D spectra bear a striking resemblance to that presented in Ref. [20], where the hole and electron masses are treated as finite.

The connection between the 2D spectra of Ref. [20] and that of Fig. 6 provides some promising avenues for future studies. The use of the modified light-matter interaction term in conjunction with the exactly solvable Eq. (1) provides a route to the study of 2D spectra that removes some of the unrealistic features of the recoilless nature of our model while preserving the ability to study the high doping limit where Fermi-polaron features should be prominent. A detailed study of this regime and the explication of the features revealed in the 2D electronic spectroscopy will be presented in future work.

The data supporting this paper are available from the corresponding author upon reasonable request.

ACKNOWLEDGMENTS

L.P.L. and D.R.R. were supported by the Chemical Sciences, Geosciences and Biosciences Division of the Office of Basic Energy Sciences, Office of Science, U.S. Department of Energy. We thank Roel Tempelaar and Timothy Berkelbach for crucial discussions.

The authors have no conflicts to disclose.

[1] D. Akinwande, N. Petrone, and J. Hone, Nat. Commun. **5**, 5678 (2014).

[2] D. Jariwala, V. K. Sangwan, L. J. Lauhon, T. J. Marks, and M. C. Hersam, ACS Nano **8**, 1102 (2014).

[3] Y. Liu, N. O. Weiss, X. Duan, H.-C. Cheng, Y. Huang, and X. Duan, Nat. Rev. Mater. **1**, 16042 (2016).

[4] A. Splendiani, L. Sun, Y. Zhang, T. Li, J. Kim, C.-Y. Chim, G. Galli, and F. Wang, Nano Lett. **10**, 1271 (2010).

[5] K. F. Mak, C. Lee, J. Hone, J. Shan, and T. F. Heinz, Phys. Rev. Lett. **105**, 136805 (2010).

[6] K. F. Mak, K. He, J. Shan, and T. F. Heinz, Nat. Nanotechnol. **7**, 494 (2012).

[7] K. F. Mak, K. He, C. Lee, G. H. Lee, J. Hone, T. F. Heinz, and J. Shan, Nat. Mater. **12**, 207 (2013).

[8] Y. You, X.-X. Zhang, T. C. Berkelbach, M. S. Hybertsen, D. R. Reichman, and T. F. Heinz, Nat. Phys. **11**, 477 (2015).

[9] G. Wang, A. Chernikov, M. M. Glazov, T. F. Heinz, X. Marie, T. Amand, and B. Urbaszek, Rev. Mod. Phys. **90**, 021001 (2018).

[10] T. C. Berkelbach and D. R. Reichman, Annu. Rev. Condens. Matter Phys. **9**, 379 (2018).

[11] Y. Zhou, G. Scuri, D. S. Wild, A. A. High, A. Dibos, L. A. Jauregui, C. Shu, K. De Greve, K. Pistunova, A. Y. Joe *et al.*, Nat. Nanotechnol. **12**, 856 (2017).

[12] M. M. Fogler, L. V. Butov, and K. S. Novoselov, Nat. Commun. **5**, 4555 (2014).

[13] Z. Wang, D. A. Rhodes, K. Watanabe, T. Taniguchi, J. C. Hone, J. Shan, and K. F. Mak, Nature (London) **574**, 76 (2019).
[14] H. Li, S. Li, E. C. Regan, D. Wang, W. Zhao, S. Kahn, K. Yumigeta, M. Blei, T. Taniguchi, K. Watanabe *et al.*, Nature (London) **597**, 650 (2021).
[15] Y. Zhou, J. Sung, E. Brutschea, I. Esterlis, Y. Wang, G. Scuri, R. J. Gelly, H. Heo, T. Taniguchi, K. Watanabe *et al.*, Nature (London) **595**, 48 (2021).
[16] T. Smoleński, P. E. Dolgirev, C. Kuhlenkamp, A. Popert, Y. Shimazaki, P. Back, X. Lu, M. Kroner, K. Watanabe, T. Taniguchi *et al.*, Nature (London) **595**, 53 (2021).
[17] K. Hao, L. Xu, P. Nagler, A. Singh, K. Tran, C. K. Dass, C. Schüller, T. Korn, X. Li, and G. Moody, Nano Lett. **16**, 5109 (2016).
[18] V. R. Policht, M. Russo, F. Liu, C. Trovatello, M. Maiuri, Y. Bai, X. Zhu, S. Dal Conte, and G. Cerullo, Nano Lett. **21**, 4738 (2021).
[19] T. L. Purz, E. W. Martin, P. Rivera, W. G. Holtzmann, X. Xu, and S. T. Cundiff, Phys. Rev. B **104**, L241302 (2021).
[20] R. Tempelaar and T. C. Berkelbach, Nat. Commun. **10**, 3419 (2019).
[21] D. K. Efimkin and A. H. MacDonald, Phys. Rev. B **95**, 035417 (2017).
[22] M. Sidler, P. Back, O. Cotlet, A. Srivastava, T. Fink, M. Kroner, E. Demler, and A. Imamoglu, Nat. Phys. **13**, 255 (2017).
[23] M. Baeten and M. Wouters, Phys. Rev. B **89**, 245301 (2014).
[24] M. Baeten and M. Wouters, Phys. Rev. B **91**, 115313 (2015).
[25] Y.-W. Chang and D. R. Reichman, Phys. Rev. B **99**, 125421 (2019).
[26] P. Nozières and C. T. DE Dominicis, Phys. Rev. **178**, 1097 (1969).
[27] J. Gavoret, P. Nozières, B. Roulet, and M. Combescot, J. Phys. France **30**, 987 (1969).
[28] N. S. Rytova, Moscow University Physics Bulletin **3**, 18 (1967).
[29] L. V. Keldysh, Pis'ma Zh. Eksp. Teor. Fiz. **29**, 716 (1979) [JETP Lett **29**, 658 (1979)].
[30] T. C. Berkelbach, M. S. Hybertsen, and D. R. Reichman, Phys. Rev. B **88**, 045318 (2013).
[31] M. R. Carbone, M. Z. Mayers, and D. R. Reichman, J. Chem. Phys. **152**, 194705 (2020).
[32] D. K. Efimkin, E. K. Laird, J. Levinsen, M. M. Parish, and A. H. MacDonald, Phys. Rev. B **103**, 075417 (2021).
[33] S. Mukamel, *Principles of Nonlinear Optical Spectroscopy* (Oxford University Press, Oxford, 1995).
[34] C. L. Smallwood and S. T. Cundiff, Laser Photonics Rev. **12**, 1800171 (2018).
[35] M. V. Durnev and M. M. Glazov, Phys.-Usp. **61**, 825 (2018).